EVALUATION AND OPTIMIZATION OF LIDAR TEMPERATURE ANALYSIS ALGORITHMS USING SIMULATED DATA

Thierry Leblanc, I. Stuart McDermid,

Jet Propulsion Laboratory
California Institute of Technology
Table Mountain Facility
Wrightwood, California 92397-0367, USA

Alain Hauchecorne, and Philippe Keckhut

Service d'Aeronomie du CNRS
BP 3,91371 Verrières le Buisson
France

Abstract

Temperature lidar data have been simulated in order to test the JPL (SO3ANL version 3.2) and CNRS/SA (TEMPER version 2.1) lidar temperature analysis software. Assuming known atmospheric temperature-pressure-density profiles, theoretical raw-photons lidar profiles have been calculated using the actual characteristics of two JPL lidar instruments, located at the Table Mountain Facility (TMF, California) and the Mauna Loa Observatory (MLO, Hawaii), and the CNRS/SA Rayleigh lidar, located at the Observatoire de Haute-Provence (OHP, France). The simulations were performed for an initial climatological profile taken from the CIRA-86 model and for various profiles derived from this model including realistic atmospheric disturbance. Comparisons between the original and retrieved temperature profiles revealed errors of several Kelvin for both the JPL and the CNRS/SA programs. By varying parameters in the simulation it was possible to determine both the source and the magnitude of these errors. Once identified the errors were corrected and the analysis programs were optimized leading to new operational versions of these programs (SO3ANL version 3.5 and TEMPER version 2.2). An accurate accounting of the temperature lidar analysis errors, before and after this work, is presented

1. Introduction,

The middle atmosphere (20- to 90-km altitude) has received increasing interest from the scientific community during the last decades, especiall y since such problems as polar ozone depletion and climatic change have become so important. Temperature profiles have been obtained in this region using a variety of satellite, rocket-, and balloon-borne instruments as well as some ground-based systems. One of the more promising of these instruments, especially for long-term high resolution measurements, is the lidar. Measurements of laser radiation Rayleigh backscattered [*Elterman*, 1951], or Raman scattered [*Moskowitz*, 1988], by atmospheric air molecules can be used to determine the relative air density profile and subsequently the temperature profile if it is assumed that the atmosphere is in hydrostatic equilibrium and follows the ideal gas law [*Hauchecorne and Chanin*, 1980]. The high vertical and spatial resolution make the lidar a well adapted instrument for the study of many middle atmospheric processes and phenomena such as gravity waves [Wilson *et al.*, 1991a; 1991 b], planetary waves and stratospheric warmings [*Hauchecorne and Chanin*, 1982; 1983], mesospheric temperature inversions [*Hauchecorne and Wilson, 1987; Leblanc et al., 1995; Whiteway et al., 1995; Leblanc and Hauchecorne, 1996],* many oscillations of various scales [*Keckhut and Chanin, 1989; 1992],* and trends [*Keckhut et al., 1993].* In recent years lidars have increasingly been used to assist in the evaluation and validation of temperature measurements from satellites, such as the Upper Atmosphere Research Satellite (UARS) [*Dudhia et al.,* 1994; *Gille et al., 1996; Fishbein et al., 1996, Hervig et al., 1996, Keckhut et al.,* 1996, *Singh et al.,* 1996] and meteorological models [Wild *et al., 1995].* In the Network for Detection of Stratospheric Change (NDSC) [*Kurylo and Solomon,* 1990] lidar is the core instrument for measuring middle atmosphere temperature profiles. Using the best lidar analysis algorithm possible is therefore of crucial importance.

In this paper, version 3.2 of the JPL lidar analysis software (SO3ANL) and version *2.1* of the CNRS/SA software (TEMPER) arc evaluated, The results of this evaluation allowed the programs to be corrected and optimized and new production software versions were produced, V3.6 for JPL and V2.2 for CNRS/SA. First, a brief description of the lidar technique for determining temperature is presented, in section 2, and then the method used to simulate lidar raw-data profiles from a given temperature profile is described in section 3. Evaluation of the JPL and CNRS/SA algorithms is discussed in section 4 and the optimization of these programs is presented in section *5.*

2. **Determination of the atmospheric temperature profile from lidar** measurements.

Laser radiation transmitted into the atmosphere, al wavelength $\lambda_{L,}$ is backscattered by molecules in the atmosphere and is collected by the lidar telescope. The number of photons received from a scattering layer δz, at a mean altitude z, is proportional to the number of photons emitted in the laser pulse and to the number of molecules or air density. If the backscattering process is Rayleigh scattering then the transmitted and received wavelengths are the same and, assuming that the only non-negligible absorption in the atmosphere is due to ozone, the Rayleigh lidar equation can be written,

$$P_R(\lambda_{L,}, z) = P_{L} \left[\beta_{Ray}(\lambda_{L}) \frac{R}{k} \rho(z) + \beta_{Mie}(\lambda_{L}) N_{Aer}(z) \right] \delta z \cdot \exp\left[-\tau_{Ray}(\lambda_{L}, z) - \tau_{O_3}(\lambda_{L}, z) \right] \frac{A_T}{(z - z_T)^2} + n_{SB} \quad (1a)$$

where $P_R(\lambda_{L,}z)$ is the number of photons received, per laser pulse, from altitude z by a telescope at altitude z_T with a receiving area, AT. PI, is the number of photons emitted in the laser pulse and β_{Ray} is the molecular cross-seetion for Rayleigh backscattering at the laser wavelength. $\rho(z)$ is the air density which is related to the number density, N, by the equation $\rho(z)=Nk/R$ where k is the Boltzmann constant and R is the mass gas constant for air (i.e., the molar gas constant divided by the air molecular weight, R*/M). β_{Mie} is the Mie backscattering ems-section for atmospheric aerosols and N_{Aer} is the aerosol concentration. The noise, n_{SB}, is the number of photons coming from the natural sky background light. The atmospheric Rayleigh extinction at the laser wavelength for the round trip between the instrument and the altitude of the measurement, z, is given by,

$$\tau_{Ray}(z) = 2\sigma_{Ray}(\lambda_{L,}) \frac{R}{k} \int_{z_T}^{z} \rho(z')\, \delta z' \quad (2a)$$

where σ_{Ray} is the wavelength dependent Ra ylcigh extinction cross-section. Similarl y, the absorption due to atmospheric ozone is given by,

$$\tau_{O_3}(z) = 2\sigma_{O_3}(\lambda_{L,}) \int_{z_T}^{z} N_{O_3}(z')\, \delta z' \quad (3a)$$

where σ_{O3} is the wavelength dependent ozone absorption cross-section and N_{O3} the atmospheric ozone number density. The ozone absorption is usually very small for most of wavelengths used to retrieved temperature.

For the Raman lidar case the backscattered wavelength is different to the transmitted wavelength, $\lambda_R \neq \lambda_L$, and the equations above must be modified to account for this. Thus, the vibrational Raman lidar equation can be written,

$$P_R(\lambda_R, z) = P_L\left[\beta_{Ram}(\lambda_L)\frac{R}{k}\rho_{N_2}(z) + \beta_{Mie}(\lambda_L)N_{Aer}(z)\right]\delta z \cdot \exp\left[-\tau_{Ray}(z) - \tau_{O_3}(z)\right]\frac{A_T}{(z - z_T)^2} + n_{SB} \quad \text{(1b)}$$

where β_{Ram} is the Raman scattering cross-section and $\rho_{N2}(z)$ is the atmospheric nitrogen density. Also, the Rayleigh and ozone extinction terms become,

$$\tau_{Ray}(z) = \left(\sigma_{Ray}(\lambda_L) + \sigma_{Ray}(\lambda_R)\right)\frac{R}{k}\int_{z_T}^{z}\rho(z')\,\delta z' \quad \text{(2b)}$$

$$\tau_{O_3}(z) = \left(\sigma_{O_3}(\lambda_L) + \sigma_{O_3}(\lambda_R)\right)\int_{z_T}^{z} N_{O_3}(z')\,\delta z' \quad \text{(3b)}$$

Since the Rayleigh extinction is far from being negligible, especially at UV wavelengths, the lidar derivation of density is a non-linear problem.

Mie scattering by aerosols is typically only important below 25-30 km and can be neglected in the equations (1a) and (1 b) for the air density derivation above 30 km. However, following volcanic eruptions particular care is required to ensure that the density derivation is not corrupted by aerosol scattering.

In a lidar system the received, backscattered radiation can be detected and measured using a photon counting system comprising a photomultiplier, pulse height discriminator and a multi-channel-scaler (MCS) for each channel. At high count rates the response of the counting system becomes non-linear, due to pulse pile-up saturation effects, and a correction has to be applied in order to obtain the true number of photons received from the observed number of photons counted, Additional y, some white and time dependent noise remains in the photomultiplier and counting system, even when no signal is received, This dark current noise, together with the natural sky background noise, has to be subtracted from the backscattered signal,

The atmospheric density can be deduced by rearranging the lidar equation (la) or (lb):

$$\rho(z) = P_R(z)\,K_L\frac{k}{R\delta z}(z - z_T)^2\exp\left[\tau(z)\right] - n(z) \quad \text{(4)}$$

where K_l, is a proportionality coefficient which includes all the atmospheric and instrumental parameters that remain constant during a measurement, and n is the total noise to be subtracted. Since K_l, is unknown, only a relative density profile can be deduced from the lidar equation. However, the temperature calculation does not need an absolute density since it is deduced from the relative density assuming hydrostatic equilibrium and the ideal gas law [Hauchecorne and Chanin, 1980], Several methods can be used to perform temperature calculat ions but they all require initialization of the profile using a reference pressure, temperature, or densit y from a model or from coincident measurements.

3. Simulation of lidar raw-data.

In order to optimize a lidar temperature algorithm it is useful to test it by analyzing simulated raw-data profiles. Starting with known, user-detincd temperature profiles the corresponding pressure and density profiles can be deduced and, in turn, theoretical or simulated raw-data profiles can be calculated using the known or measured characteristics of any specific lidar instrument. Simulated raw-data profiles are generated and then analyzed using the standard analysis algorithms as though they were measured profiles. The 'retrieved' temperature profiles are compared to the 'original' simulated ones. In this section, the simulation process is discussed and comparisons between retrieved and the original profiles will be presented in section 4.

The first step in the data simulation procedure is the creation of the initial temperature profile. The CIRA-86 model [*Barnett et al,* 1990; *Fleming et al*, 1990] was chosen as the climatological reference and as the starting point for the generation of test profiles. This model includes the zonal and monthly mean temperature between O- and 100-km and the components of the planetary waves of wavenumber 1 and 2. The January-mean CIRA-86 temperature profile at 44°N, 6"E was chosen as the basic reference profile, Various disturbances to this profile were introduced to simulate non-climatological profiles for the case studies described below.

The second step is to create the pressure-density profile associated with the generated temperature profile. A pressure (or density) reference is needed in order to compute these profiles which is done using the hydrostatic equilibrium and ideal gas law. A pressure value of 2,7 hPa at the geometric altitude of 40 km was taken, which is close to the climatological value. The altitude of the pressure reference can play a significant role in the interpretation of some temperature comparisons, as explained in section 4. The simulated interdependent temperature-pressure-derrsit y profile is then used

to compute the theoretical number of photons that would be received by a given lidar instrument taking into account the known parameters of that instrument, This is the main part of the simulation process.

The Rayleigh lidar equation (1a) is evaluated, considering only the atmospheric backscattering and the constant terms relevant to the entitling system. This corresponds to the backscattered signal and the equation takes the form,

$$S_0(\lambda_L, z) = P_L(\lambda_L)\,\beta_R(\lambda_L)\frac{R}{k}\rho(z)\delta z \qquad (5)$$

The Rayleigh extinction and ozone absorption corrections are then applied to the signal for the round-trip of the light between the instrument and the altitude of measurement:

$$S_1(\lambda_L, z) = S_0(\lambda_L, z)\exp\left[-\tau_{Ray}(z)\right]\exp\left[-\tau_{O_3}(z)\right] \qquad (6)$$

Two redundant methods of Rayleigh extinction correction were introduced to avoid any numerical problems relevant to computer precision. The first simply evaluates equation (2a) using the density as a function of altitude. The second method first uses the pressure at the surface, $p(z_T)$, to calculate the extinction to the top of the atmosphere, $p(z_\infty)=0$. Then, the extinction between the altitude of the measurement, at pressure p(z), and the top of the atmosphere is calculated. The difference between these two values is the required extinction between the surface and the altitude of the measurement. This method can have some advantages in real situations when the surface pressure is highl y variable.

$$\tau_{Ray}(z) = \sigma_{Ray}(\lambda_L)\frac{R}{k\,g}p(z_T) - \sigma_{Ray}(\lambda_L)\frac{R}{k\,g}p(z) \qquad (7)$$

Both methods give similar results, which shows that on the onc hand that no precision errors arc introduced when using very small or very large constants such cross sections or Boltzmann constant in the extinction correction, and on the other hand that the temperature calculation depends onl y on the relative and not absolute density (the results of both methods differ only by a proportionality constant). An ozone absorption correction was also introduced in case of absorbed wavelengths using an ozone density taken from climatology. The wavelength dependence of the ozone absorption cross section in the Chapuis band, centered on 590 nm (Brasseur and Solomon, 1986), was considered in this correction. If lidar wavelength shorter than 340 run are used then absorption due to the Hartley band and temperature dependent Hug gins band of ozone must be considered.

The simulations performed here assume that no aerosols contribute to the signal extinction or backscattering. Therefore, it should not be surprising to see, in section 4, comparisons of Rayleigh temperatures well below 30 km.

Since only a fraction of the incident backscattered signal is received on the telescope area, it has to be corrected by the corresponding solid angle formed between the altitude of measurement and the telescope surface. The range correction to be applied is,

$$S_2(\lambda_{1,}, z) = S_1(\lambda_{1,}, z) \frac{A_T}{(z - z_T)^2} \tag{8}$$

The noise from the sky background light must bc added to the signal but since it is not backscattered is obviously not range corrected. However, when several i ndependent channels arc used for analyzing the lidar temperature, the sky background noise should bc normalized by the fields-of-view (fov) of the telescopes if they are different. Also, some correction may bc necessary for a non-negligible effect of misalignment or incomplete overlap, $\xi(z)$, of the emitting and receiving systems if the backscattered signal is not completely included in the telescope fov. For the current simulations, no correction is introduced since the fov are assumed to be wide enough to receive the backscattered signal from all the measured altitudes (10- to 100-km), i.e., $\xi(z)= 1$.

$$S_3(\lambda_{1,}, z) = S_2(\lambda_{1,}, z)\,\xi(z) + n_{SB} \tag{9}$$

The signal and sky background light are then transmitted between the receiving and counting systems. An efficiency coefficient has to be introduced to account for the optical transmission between the telescope surface and the photomultiplier detectors. An additional quantum efficiency coefficient is applied to finally obtain the simulated number of photo-electrons received on the counting system, and ready to be counted.

$$P_R(z) = S_3(\lambda_{1,}, z)\, t_T\, t_G\, t_F\, \eta_Q \tag{10}$$

t_T is the telescope transmission, t_G the transmission along the optical path, t_F the transmission of the filters and η_Q the quantum efficiency of the photomultiplier.

The photomultiplier and the counting system then translate the photons received into electronic pulses which are counted by the MCS. Due to the high dynamic range of the signal (10-4 to 10^5 photons/pulse/microsecond, depending on the altitude) the system can be either saturated if too many photons arrive in a short period or under-saturated if the magnitude of the electronic pulse caused by a low signal is too small to be retained [see for example, *Donovan et al.*, 1993]. The number of photons

counted is therefore different from the true number of photons received. The correction applied is function of the maximum counting rate of the electronics, and the level of discrimination of the electronic pulses. The following law, taken from statistical studies [Donovan *et al.*, 1993] was used,

$$P_C(z) = (1-u)\,P_R(z)\exp\left[-\frac{P_R(z)}{c\,P_{max}}\right] + \left(u-u^2\right)P_R^{\,2}(z)\exp\left[-\frac{P_R(z)}{c\,P_{max}}\right] \qquad (11)$$

where $P_C(z)$ is the number of photon counts observed, P_{max} is the maximum number of photon counts that are observed when the system fully saturates (note, $c\,P_{max}$ corresponds to the maximum specified count rate of the system), and u is the discriminator level (0 if all the electronic pulses are counted, 1 if no pulses are counted). This equation is a second order approximation of an equation with an infinite number of terms. If one takes 0 for the discriminator level (which is a good approximation in most cases), this equation becomes a first order approximation of the theoretical one, and is written,

$$P_C(z) = P_R(z)\,C\exp\left[-\frac{P_R(z)}{c\,P_{max}}\right] \qquad (12)$$

which is more easily inverted by the lidar analysis algorithms.

Finally, an instrumental noise $n_I(z)$ has to be added. This so called signal-induced-noise is a reaction of the photomultipliers to the very strong signal received from the lower altitudes which results in a time dependent enhancement of the background counts. It can usually be fitted by an exponential, polynomial or linear function of altitude depending on its severity or magnitude. Polynomial functions (degrees 0 to 2) were used to create the simulated instrumental noise.

$$\mathbf{P(z) = P_C(z) + n_I(z)} \qquad (13)$$

The number of photons finally obtained P(z) is assumed to be the raw-data, as if it was really measured by the instrument. The data files are formatted to be read by the different lidar algorithms. They are analyzed and the temperature results are compared to the original simulated profiles. In the next section, these comparisons are presented.

It should be noted that the various proportionality constants applied to the simulated signals are not really necessary since the lidar temperature algorithms retrieve a relative density. However, the output data of the simulation software must present signal levels similar to those obtained with real measurements since the analysis algorithms typically use these levels in various steps of the temperature derivation. To ensure that the results were not dependent on the simulations themselves, the latter were performed using characteristics typical of several different lidar systems.

The simulation of vibrational Raman lidar temperature measurements was also performed. The methods and equations used are similar to the Rayleigh simulation, except for few points. The nitrogen density is retrieved instead of air density, the backscattered wavelength is different from the emitted wavelength $(\lambda_R \neq \lambda_L)$, and the Raman cross sections arc different from the Rayleigh cross sections. Only the results from the Rayleigh simulation will be shown, since the results for the Raman case are strictly similar.

4. Evaluation of the JPL and CNRS/SA temperature lidar algorithms.

In this section the simulation procedure described above is used to evaluate the temperature retrieval algorithms of the JPL and CNRS/SA lidar systems, and to diagnose inaccuracies or identify limitations in these analysis methods. The initial software versions tested were V3.2 of the JPL SO3ANL program and V2. 1 of the CNRS/SA TEMPER program. This latter, an upgraded version of TEMPER V1.x, was recently rewritten for a new UNIX environment and had not yet proceeded to archive data. Simulation were performed taking into account the actual characteristics of three different lidar systems: the Table Mountain Facility (TMF, 117.7GW, 34.4°N) and Mauna Loa Observatory (MLO, 155.6°W, 19.5°N) lidars of JPL, and the Observatoire de Haute-Provence (OHP, 6°E, 44°N) Rayleigh lidar system of CNRS/SA, France. The characteristics of these lidars, used in the simulations, are shown in table 1.

	MLO	TMF	OHP
Longitude	155.6° W	117.7" w	6.0° E
Latitude	19.5° N	34.4° N	44.0° N
Altitude (m)	3400	2300	685
Vertical resolution (m)	300	300	75
Altitude Range (km)	15-90	25-85	20-100
Number of Rayleigh channels	1	1	2
Number of Raman channels	1	0	0
Wavelength (Rayleigh) (rim)	353	353	532
Wavelength (Raman) (rim)	385		
Laser energy (mJ/pulse)	50	50	300
Laser frequency (pulse/s)	200	150	50
Telescope area (m^2)	0.78	0.64	0.78/0.03
Field of view (mrad)	1.0	2.0	0.25/0.55
Optical transmission	0.21	0.21	0.21
Quantum efficiency	0.25	0.25	0.18
Counting rate (Max, MHz)	250	250	150
Discriminator level	- o	- o	- o

Table 1: Characteristics of the lidar instruments used in these simulations for retrieving temperature.

In order to make ideal comparisons it was assumed that all the instruments were located exactly at the same site so that the same reference profiles could be used. This assumed location was 6"E, 44°N, i.e., that of the OHP lidar. However, the elevations of each instrument at their actual sites were retained to keep the correct magnitude of signal and noise levels. Because the same analysis software is used for both TMF and MLO lidar systems, only MLO results will be shown, together with the OHP results.

As a starting point, a standard CIRA [*Barnett et al, 1990; Fleming et al, 1990]* temperature profile was used in the raw-data simulation. Since the lidar algorithms necessarily use model information in at least one part of the analysis, a simulated profile taken from a climatological model allows the study of analysis errors independent of the model errors. Raw data profiles corresponding to the CIRA-86 temperature profile at 44°N, 6°E in January were simulated and retrieved, The simulated temperature profile obtained here is an ideal case and it contains no small scale disturbances. However, realistic experimental noise was included in the raw-data profiles to simulate a real data acquisition, **Figure** 1 shows the original CIRA temperature profile (left plot) and the deviation between this profile and the OHP (center) and MLO (right) retrieved profiles. The dotted lines indicate the one-sigma standard

deviation associated with the retrieved profiles. Both retrieved profiles remain close to the original, at least below 70 km, with an increasing standard deviation at higher altitudes due to the statistical noise introduced. The MLO profile is systematically cut-off at 80 km, while the OHP profile is cut-off at a given signal to noise ratio, Some significant differences between the original and retrieved profiles appear below 40 km for both the JPL and CNRS/SA profiles. These departures are much greater than the one sigma standard deviation, especially for the JPL profile below 25 km and indicate that there are some problems with the present versions of the algorithm...

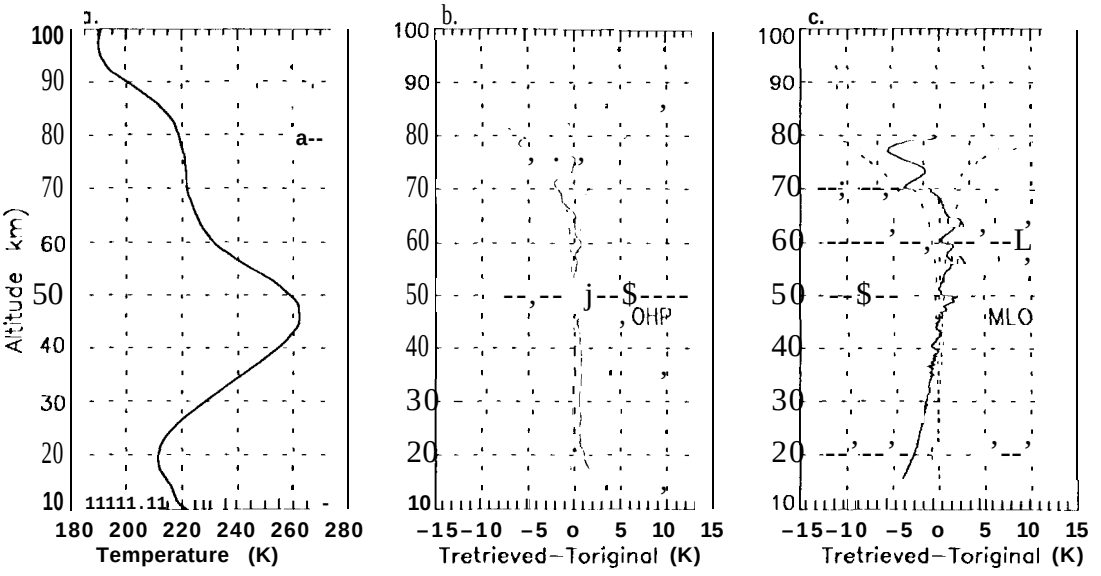

Figure 1: Simulated (CIRA-86 at 44*N, 6°E) temperature profile (a), and deviation between this profile and the OHP (b) and MLO (c) retrieved profiles. The MLO lidar analysis assumes that the instrument is located at 44°N, 6"E. The dotted lines indicate the temperature error at one standard deviation.

To help identify the source(s) of the errors leading to such departures the same profile was simulated but without instrumental noise. Figures 2(a) and (b) are similar to figures 1(b) and (c), except that the instrumental noise was suppressed. Now, the shape of the departures is much clearer, and the departures are apparently of different origin for OHP and MLO.

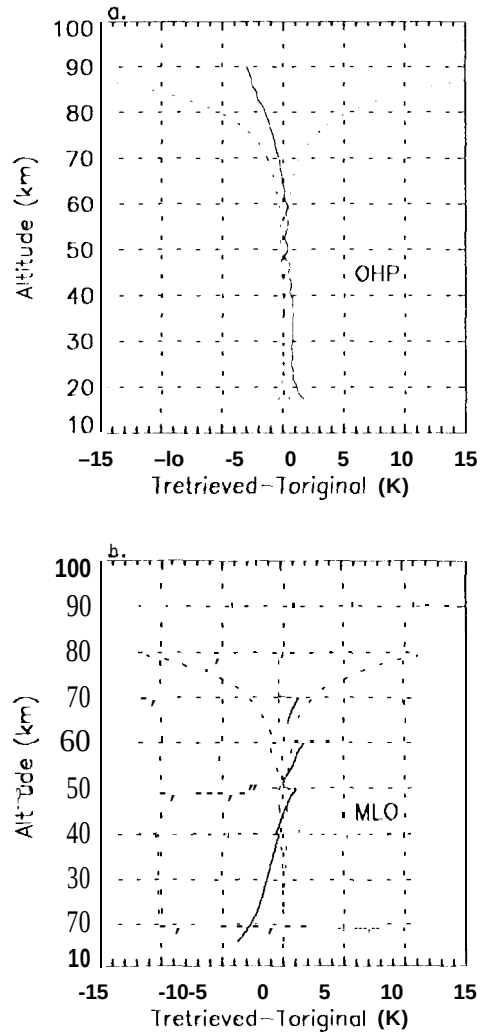

Figure 2: Same as figure 1 (b) and (c), but with no instrumental noise in the simulated raw data.

Large steps are observed every ten kilometers on the MLO profile in figure 2 which were not clear on the previous figure. These steps were easily identified as being related to the smoothing part of the algorithm since they occur at the altitude% every ten kilometers above 40 km, where the vertical smoothing range was increased. Review of the JPL algorithm revealed that a linear smoothing function was applied to the density signal which is actually an exponential function, decreasing with height. This source of inaccuracy was removed by applying the same smoothing method to the logarithm of the density which can be considered as a nearly linear function of altitude. Repeating the analysis with the corrected smoothing routine gives the result shown in **figure** 3 where it can be seen that the steps have completely disappeared.

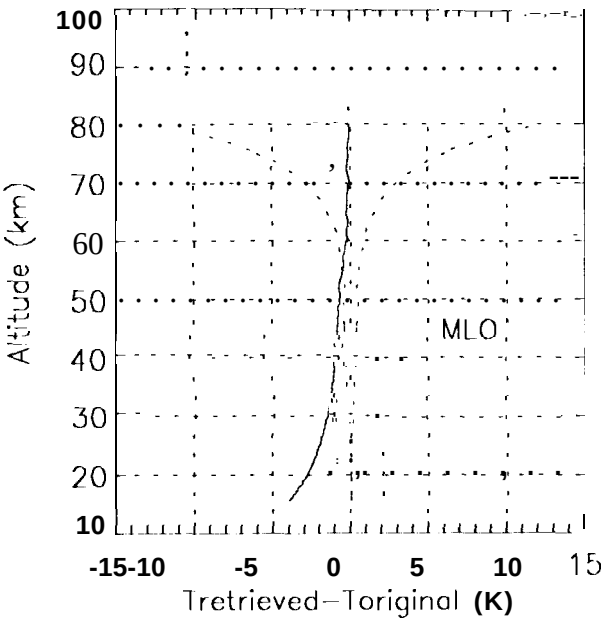

Figure 3: Same as figure 2b, but smoothing $\log(\rho)$ instead of ρ.

Now, the departure from the original profile is a continuous function of altitude, increasing to lower altitudes, Looking at the algorithm in detail, it was noted that the instrument altitudes, z_T, were slightly offset from their true values, for both MLO and OHP. This error results from some confusion created when altitudes preassigned to the top, bottom, and center of time bins in the MCS. By correcting this altitude, the solid angle correction given by equation (8) is different. The results obtained when the correct instrument altitudes were used is shown in figure 4.

The improvements to the MLO profile in figure 4(b) is spectacular and the maximum difference between the original and received profiles is -0.5 K, at the very bottom of the profile. For OHP however, a departure of -1.5 K at 18 km, and -3 K at the top still remains. The bottom departure appeared to be due to the correction applied to account for ozone absorption of the laser and backscattered radiation. The ozone vertical distribution used to compute the Chapuis band ozone absorption (equation 3b) in the simulation software differed from that in the OHP analysis software by a multiplicative factor of 2 and the effect on the corrected signal is not negligible at 532 run, This error can not occur at UV wavelengths, $340<\lambda<400$ nm, since the ozone absorption there is negligible, The factor of 2 in the OHP algorithm appeared to be a mistake and when this was corrected the profile plotted in figure 5(a) was obtained. The differences at the bottom of the profile are now completely removed and remain inside the ± 0.4 K error bars at 18 km, similar to the MLO analysis.

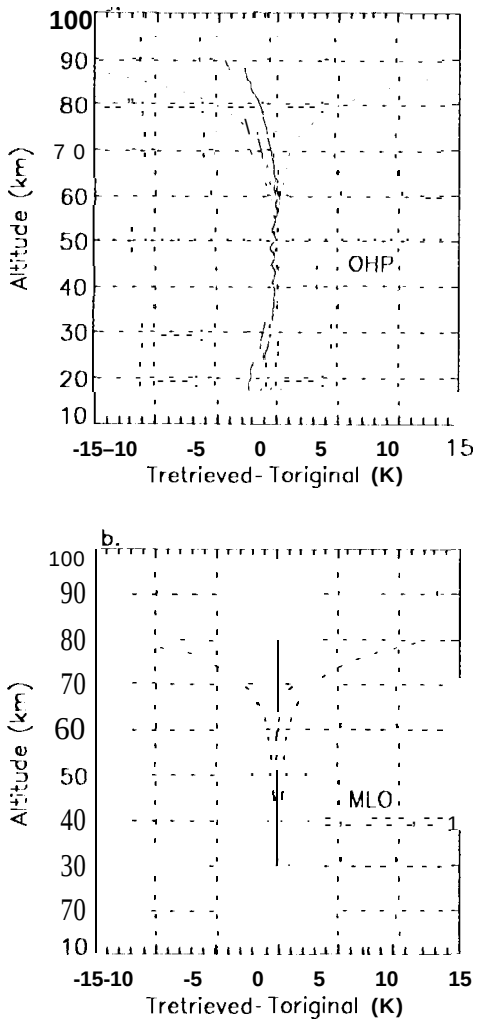

Figure 4: Same as figures 2(a) and 3, **but** using the revised site altitude and solid angle correction,

Now, the last significant difference observed in **figure** 5(a) is for OHP **at** the top of the profile (3 K at 90 km). This departure is related to the methodology of the background noise estimation and subtraction, In **figure** 5(a) a second order polynomial function was used in the simulated data **to** represent the signal induced noise and a polynomial tit was applied in the OHP **retrieval. In figure** 5(b) a linear function was introduced in the simulated data and a linear fit was applied in the OHP retrieval, This demonstrates that the error is introduced by the method used to fit the shape of the **signal-induced-**noise and that the linear **fit** is more accurate. Unfortunately, a linear fitting function is not applicable for all systems because the signal-induced-noise has a different functional dependence on altitude because of instrument specific factors. A linear **fit** is adequate for the MLO system, but a polynomial or exponential fit is more appropriate for the TMF and OHP **lidars**.

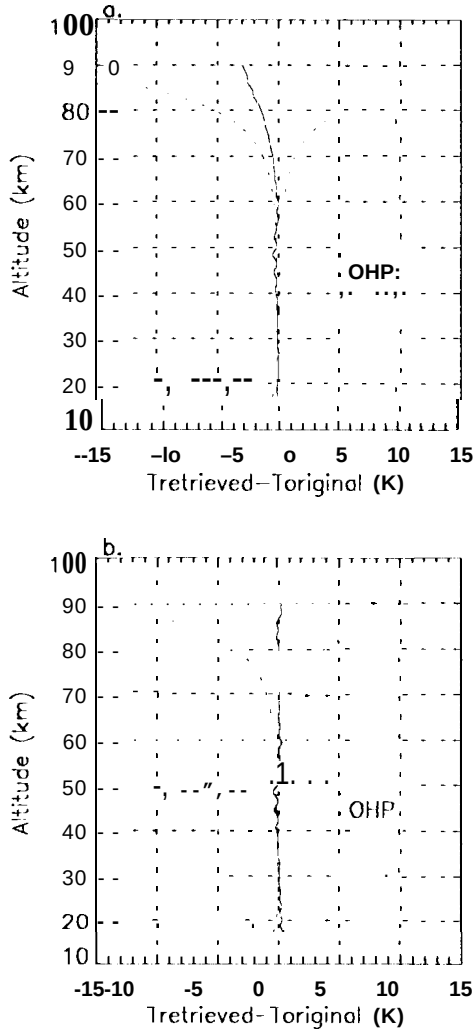

Figure 5: a) Same as figure 4(a), but with a corrected ozone profile for absorption in the Chapuis band. b) Same as (a) but with a linear fit used for the background noise extraction instead of a 2nd-degree polynomial.

Evaluating the temperature deviations between the original and retrieved profiles, in **figure** 5(b) for OHP and figure 4(b) for MLO, it appears that all significant errors have been identified and corrected,

5. Optimization of the JPL and CNRS/SA temperature lidar algorithms.

In this section the simulation is used to optimize the temperature retrievals of the JPL and CNRS/SA lidar systems. We will focus on two subjects: The effect of introducing *a priori* information into the instrumental data, and the effect of smoothing. We also show at the end of this section the effect of introducing a purposely inaccurate determination of altitude measurement.

For lidar temperature retrievals, *a priori* information is necessary at two different steps in the data processing:

1) when normalizing the signal (relative density) to an *a priori* density:

$$p(z) = S(z)\,\frac{\rho_{ref}}{S(z_{ref})} \tag{14}$$

where ρ_{ref} is taken from a CIRA-like climatological model or from a NMC-like assimilation model. For both models, the accuracy of the reference density value, and the altitude of normalization, are of crucial importance.

2) when starting the downward integration of the temperature profile from the top.

Figures 6 and 7 illustrate, using the MLO retrieval as an example, two dramatic consequences of the *a priori* need. Figure 6 is similar to figure 4(b) but the density normalization is different.

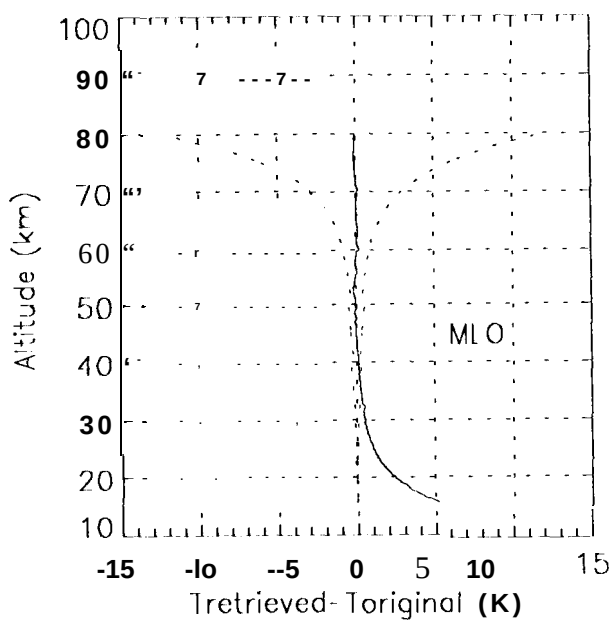

Figure 6: Deviation between the simulated (standard CIRA) and the MLO retrieved profile when the a *priori* reference density for normalization at 16 km is 10% different from the simulated density. See figure 4(b) for the same profile obtained using a normalization at 40 km with the exact CIRA reference density.

In figure 4(h) the *a priori* reference density was roughly the same as that of the simulated (CIRA) profile, taken at 40 km, while in figure 6, a 10% error was purposely introduced in the *a priori* value of the density and purposely normalized at the bottom of the profile(16 km). If the *a priori* value of the density was exactly the same as the CIRA value, this error would not have appeared. Also, it would

have been much smaller if the same 10% relative error had been introduced for a normalization at 40 km since the absolute value of the density is more than 30 times smaller at this altitude. With a 10% relative error in the density at 16 km, the error in calculating the Rayleigh extinction correction (using the absolute density) is far from being negligible, especially at UV wavelengths, and leads to the 5 K departure at 16 km observed in **figure** 6. An altitude of 40 km is in fact a good compromise since the instrumental noise increases and the confidence in the models decreases with height, and since saturation and aerosols can affect the signal at lower altitudes.

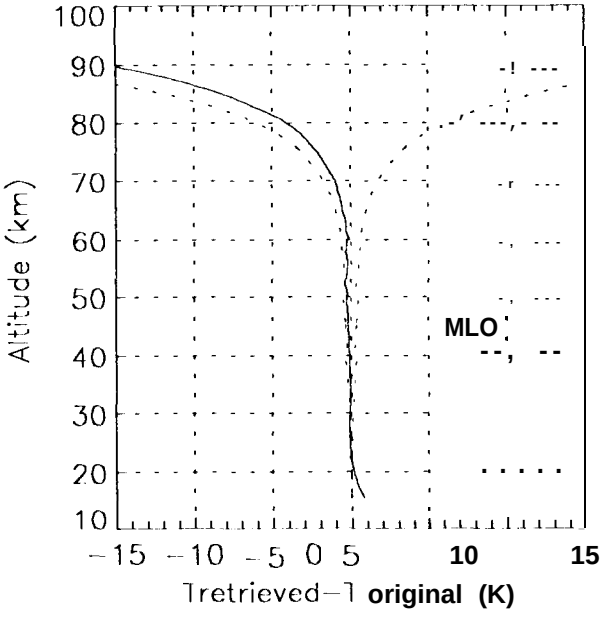

Figure 7: Deviation between original and MLO retrieved profiles for a simulated profile 15 K warmer than the standard CIRA profile.

Figure 7 illustrates, again using the MLO retrieval as an example, the effect of the temperature initialization at the top of the profile, The lidar temperature retrievals always need such an initialization, which can be made by taking an *a priori* temperature and density or pressure at the top. The temperature profile is then integrated downward, using one of the two following redundant equations:

$$T(z_i) = \frac{1}{\rho(z_i)}\left[\rho_{TOP}\, T_{TOP} + \frac{M\, g(z_i)\, \delta z}{k} \sum_{z_i}^{z_{TOP}-1} \rho\left(z_i + \delta z/2\right) g\left(z_i + \delta z/2\right) \right] \qquad (15)$$

$$T(z_i) = \frac{\delta z\, g(z_i)}{R\left(\ln\left(p(z_i - \delta z/2) \right) - \ln\left(p(z_i + \delta z/2) \right) \right)} \qquad (16)$$

In the case of figure 7, the simulated profile is 15 K warmer than the CIRA profile at all altitudes. Therefore, when initializing at 90 km to the CIRA temperature, T_{TOP}, a -15 K departure is observed. Then, the error quickly decreases as we integrate downward because of the quasi-exponential growth of the density. Starling with a 15 K error at 90 km, it drops to 4 K at 80 km and 1 K at 70 km and becomes negligible below this. Although the error due to the *a priori* density normalization can be reduced, the error due to the initialization at the top can not be removed, This can be a significant limitation of the lidar temperature analysis, especially near the mesopause which is a region with large temperature variability.

It should be noted that figure 7 illustrates the worst condition of using the *a priori* information since real temperature profiles are never 15 K hotter than the climatology throughout the entire profile (15-90 km). Even if deviations of 25-30 K occur at mesospheric heights, small vertical scale wave structures allow the real temperature to reach climatological values in several kilometers, making the convergence from the outlying *a priori* values to the real values much faster.

Another source of error which can be identified using simulated data is the vertical smoothing. The errors associated with the smoothing are usually small, and are maximum where the vertical temperature gradient changes quickly with altitude. For this reason wc simulated a CIRA profile with a typical strong mesospheric temperature inversion added. These so called "temperature inversions" are frequently observed, especially at winter mid-latitudes at about 70 km altitude [Leblanc et al., 1995], [Leblanc and Hauchecorne, 1997], Figure 8 shows the simulated profile (a) together with the deviations between this profile and the OHP (b) and MLO (c) retrieved profiles. The retrieved profiles were obtained using the improved version of each software (i.e., the versions obtained at the end of the section 4). For both instruments, the maximum deviation occurs in the region of inversion of the vertical temperature gradient (± 1 to 1.5 K at 67 and 73 km). The magnitude of the departure depends on the vertical scale of the smoothing which, in turn, is related to the signal levels.

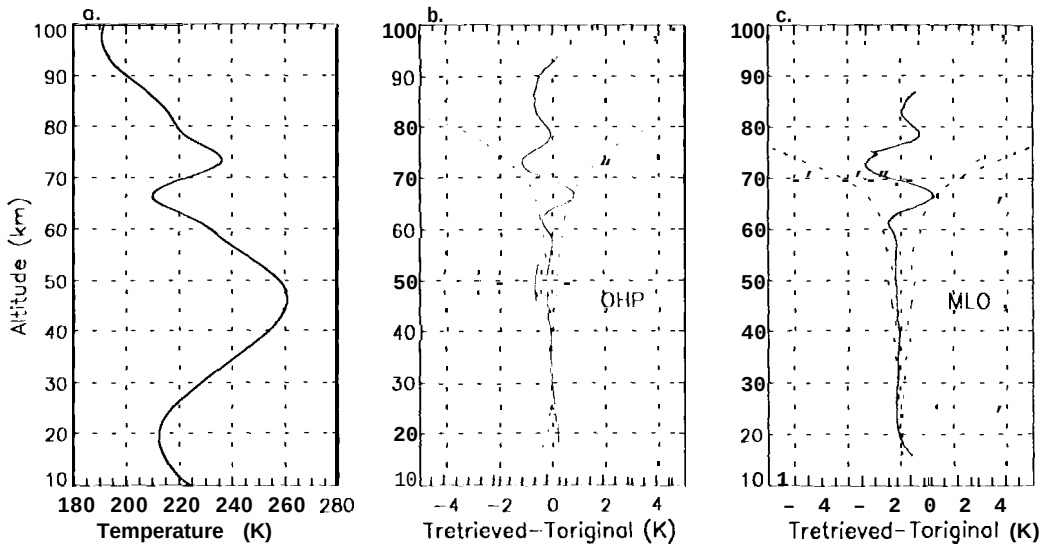

Figure 8: Simulated standard CIRA profile including a mesospheric temperature inversion (a) and deviation between this profile and the OHP (b) and MLO (c) retrieved profiles.

Figure 9 points out the dependence of this departure on the second vertical derivative of the temperature. The crosses correspond to the MLO retrieved profile and the circles to the OHP retrieved profile. The dependence is quasi-linear and makes it very easy to evaluate the magnitude of the error due to the smoothing for a given profile. The maximum of departure is about ± 1.3 K for MLO, and ±1.2 to 0.9 K for OHP, occurring exactly at the bottom ($\delta^2T/\delta z^2$ = +2.2 K/km^2) and top ($\delta^2T/\delta z^2$ = -2.2 K/km^2) of the temperature inversion, The straight lines are not strictly centered on zero (-0.3 K offset) due to the general shape of the temperature profile (large vertical scale effect) but the departures are very well centered to this offset, The slope of the straight lines determines the degree of accuracy of the smoothing method. This latter is given by the initial vertical resolution and the vertical smoothing window on the one hand, and by the smoothing algorithm on the other hand. The selection of either a constant or a variable vertical smoothing range rests on a compromise between altitude resolution and error limits and the optimum choice is dependent on the nature of the application of the temperature results. For OHP, a constant 4.65 km vertical Hamming window is applied to the initial 75 m resolution, For MLO, a variable window (1 km to 8 km) low-pass filter is applied to the initial 300 m resolution. At the altitude of the temperature inversion, this window is 6 km below 75 km, and 8 km above, making the slope of the straight line and the extrema larger than for OHP. This kind of plot easily allows the magnitude of the errors due to the smoothing to be determined.

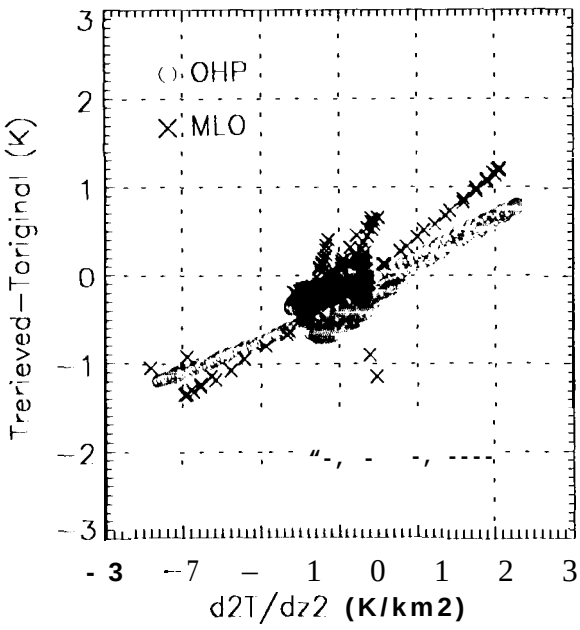

Figure 9: Deviation bet ween the retrieved and the original profiles as a function of the second vertical temperature derivative, for OHP (circles) and ML() (crosses).

Similar plots are useful to identify another source of error, namely an inaccurate altitude determination, which is not always observable when plotting profiles, even when using simulated data. **Figure 10** (a and b) shows the deviation between original and retrieved profiles as a function of the vertical temperature gradient, for the same simulated profile as used in figure 8(a), for two different cases. In **figure** 10(a) the determination of altitude measurement is correct. The zero value of $\delta T/\delta z$ corresponds to the extrema of the second derivative shown in the previous figure. The plot is a horizontal ellipse and the maximum deviation, **due** to the vertical smoothing, occurs near the zero vertical temperature gradient. In **figure** 10(b) a 600 m offset (typically 2 consecutive data points for the JPL instruments) was purposely introduced in the determination of altitude measurement. Consequent y, the ellipse becomes inclined with the altitude shift acting as a phase-delay between the vertical temperature gradient and the departure **due to the smoothing**. The deviation bet ween retrieved and original profiles has dramatically increased, the extrema now occurring at the ends of the long axis of the ellipse, instead of occurring at the ends of the short axis. No such evidence of altitude shift is observable when one simply compares the simulated and retrieved temperature profiles, especiall y when this shift is small.

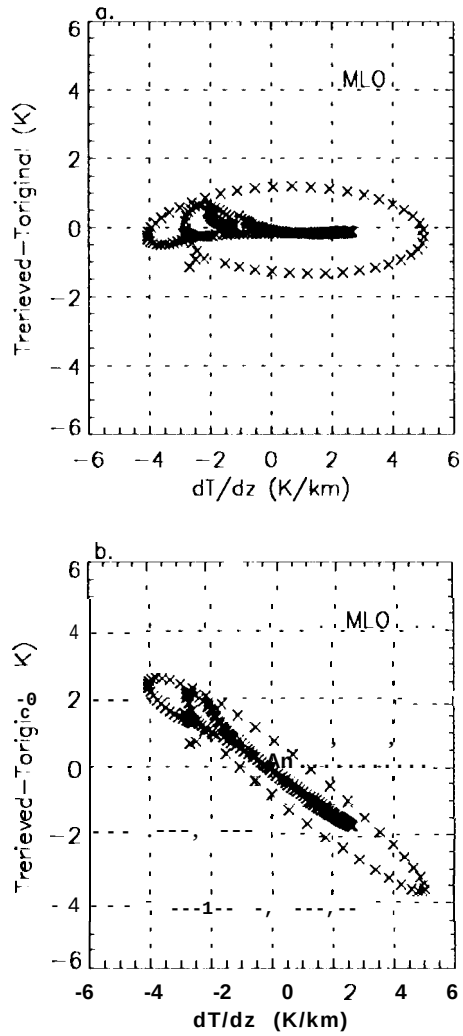

Figure 10: Deviation between the original and MLO retrieved profiles as a function of the vertical temperature gradient, Top: with a correct determination of the altitude of measurements. Bottom: with a 600 m (2 points) error in the determination of the altitude of measurements.

6. Conclusion.

The use of simulation has been shown to be useful for testing the lidar analysis algorithms. Using known temperature-pressure-density profiles some typical raw-data profiles were simulated and then analyzed by different lidar soft wares as if they had been obtained by real measurements. The retrieved temperature profiles were then compared to the simulated original profiles. By using different analysis methods, or by purposely introducing inaccuracies, the effects on the error related to different parts of the lidar analysis could be determined. Different error sources have been identified and quantified and are summarized in table 2.

	16km	40 km	top - 10 km	top (~ 95 km)
450 m error in instr. altitude	2.5% -5 K	0.6% -1.5 K	Near Zero	Near Zero
50% error in 03 absorption (532 nm)	0.8% - 1.5 K	0.08%- 0.2 K	Near Zero	Near Zero
Background extraction:				
Max effect:	Near Zero	Near Zero	1% - 1.5 K	2% - 3 K
Min effect:	Near Zero	Near Zero	Near Zero	Near Zero
1 % err. in reference density				
Normalization At 16 km	1% - 2 K	Near Zero	Near Zero	Near Zero
(353 nm) At 40 km	Near Zero	Near Zero	Near Zero	Near Zero
10% err. in reference density				
Normalization At 16 km	2.5% -5 K	0.04%- 0.1 K	Near Zero	Near Zero
(353 nm) At 40 km	0.3% -0.6 K	Near Zero	Near Zero	Near Zero
10% err. in reference density				
(532 nm) Norm. At 40 km	Near Zero	Near Zero	Near Zero	Near Zero
15 K error on temperature initialization using model	Near Zero	Near Zero	2% - 4 K	12% - 15 K
Smoothing effect vs. $\delta^2T/\delta z^2$	O K/km^2	1 K/km^2	2 K/km^2	
Hamming vertical window: 4.65 km	Near Zero	0.5 K	1 K	
Low pass filter vertical window: 6.0 km	Near Zero	0.7 K	1.4K	

Table 2: Summary of the relative and absolute errors from the lidar temperature analyses, identified using simulated data.

For quasi-climatological profiles, the most important error is due to the smoothing (maximum deviation of 2 K). When the simulated profile is far from a climatological profile the most dramatic departures are located in the first 10 kilometers from the top due to the necessary initialization by model data (20 K departure of temperature is frequently observed). The accuracy of the background subtraction is of crucial importance if one wants to make the profiles rapidly converging to the true temperature. A secondary effect is the inaccurate normalization of density, used in the extinction correction at UV wavelengths, leading to departures up to 3 K at the very bottom for UV wavelengths. Finally, range correction errors or altitude shifts can lead also to significant departures in the lower part of the profiles.

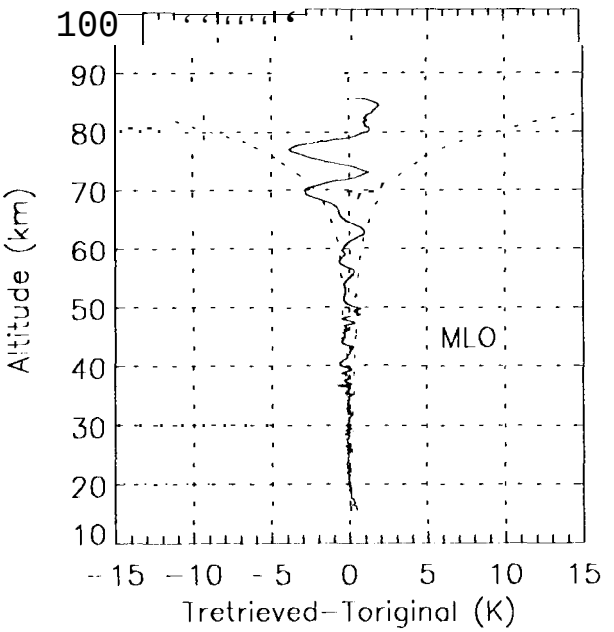

Figure 11: Same as figure lc, but after use of the simulation, and the subsequent improvements of the analysis soft ware.

The use of simulation has allowed the identification of several typical errors occurring when using the lidar analysis. Figure 11, obtained after evaluation and optimization of the JPL temperature analysis software using the simulation, should be compared with figure l(c). It illustrates the usefulness of such approach. The optimization of cut-off and error calculations is clear at the top. The improvement of the smoothing is clear at 70, 60 and 50 km. The effect of inaccurate range correction, leading to a 2 K too cold at 25 km, disappeared. At last, a better density normalization makes the lower stratospheric retrieved temperature (15 to 25 km) much closer to the original temperature. Table 3 summarizes the temperature error and range resolution of the JPL and CNRS/SA algorithm before and after the evaluation and optimization carried out in this study.

Other useful tests, concerning notably noise and saturation correction effects, can be investigated in the future simulations. In addition, it may be important to introduce the effect of the aerosols layer in order to come as close to real measurements as possible.

	MLO				TMF				OHP			
	V 3.2		V3.5		V 3.2		v 3.5		v 2.1		v 2.2	
Altitude (km)	Err (K)	Ran (km)	Err (K)	Ran (km)	Err (K)	Ran (km)	Err (K)	Ran (km)	Err (K)	Ran (km)	Err (K)	Ran (km)
15 (Raman)	>5	3	1	1	-	-	-	-	-	-	-	-
30 (Raman)	4	3	4	2	-	-	-	-	-	-	-	-
30	2	1	<0.5	1	2	1	<0.5	1	1	4.65	<0.5	4.65
40	2	1-2	<0.5	1-2	2	1-2	<0.5	1-2	cl	4.65	<0.5	4.65
60	1	4-6	1	4-6	2	4-6	2	4-6	<1	4.65	<1	4.65
80	15	6-8	10	8	20	6-8	20	8	5	4.65	5	4.65
90			20	8	-	-	-	-	20	4.65	20	4.65

'l'able 3. Summary of the temperature error and range resolution before and after the evaluation and optimization carried out in this study.

The simulations presented in this paper have demonstrated the capability to evaluate lidar temperature anal ysis programs and to diagnose typical problems. Application of this technique to evaluate the different temperature analysis programs used by most of the lidar groups within the NDSC is planned.

Acknowledgments

The work described in this paper was carried out at the Jet Propulsion Laboratory, California Institute of Technology, under an agreement with the National Aeronautics and Space Administration. TL is grateful to the National Research Council for the award of a Research Associateship. We arc grateful to Eric Sirko (JPL), J-P. Marcovici, F. Pinsard, A. Sauron, and P. Lieutaud (CNRS/SA) for assistance with the anal ysis programs.

References:

Barnett, J. J., and S. Chandra, COSPAR International Reference Atmosphere, Chapter 1: Atmosphere Grand Mean, *Adv. Space Res., 10,7-10,* 1990.

Donovan, D, P., J. A. Whileway, and A. 1. Carswell, Correction for non-linear photon-counting effects in lidar systems, *Appl. Opt., 32, 6742-6753,* 1993.

Dudhia, A., N. J. Livesey, and F. W. Taylor, Validation of ISAMS Retrievals of atmospheric temperature and pressure, *Adv. Space Res., 14, 237-241,* 1994.

Elterman, L. B., The measurement of stratospheric density distribution with the searchlight technique, *J. Geophys Res.,* 56,509-520, 1951.

Fishbein, E. F., R. E. Cofield, L. Froidevaux, R. F. Jarnot, T. Lungu, W. G. Read, Z. Shippony, J. W. Waters, I. S. McDermid, T. J. McGee, U. Singh, M. Gross, A. Hauchecorne, and M. E. Gelman, *J. Geophys. Res., 101,9983-10,016,* 1996.

Fleming, E. L., S. Chandra, J. J. Barnett, and M. Corney, COSPAR International Reference Atmosphere, Chapter 2: Zonal Mean Temperature, Pressure, Zonal Wind, and Geopotential Height as a Function of Latitude, *Adv. Space Res., 10,* 11-59, 1990.

Gille, J. C., P. L. Bailey, S. T. Massie, L. V. Lyjak, D. P. Edwards, A. E. Roche, J. B. Kumer, J. L. Mergenthaler, M. R. Gross, A. Hauchecorne, P. Keckhut, T. J. McGee, I. S. McDermid, A. J. Miller, and U. Singh, Accuracy and precision of cryogenic limb array etalon spectrometer (CLAES) temperature retrievals, *J. Geophys. Res., 101,9583-9602,* 1996.

Hauchecorne, A., and M. L. Chanin, Density and Temperature Profiles obtained by lidar between 35 and 70 km, *Geophys. Res. Lett., 8,* 565-568, 1980.

Hauchecorne A., and M. L. Chanin, Mid latitude ground-based lidar study of stratospheric warnings and planetary waves propagation, *J. Atmos. Terr. Phys., 44, 577-583, 1982.*

Hauchecorne A., and M. L. Chanin, Mid latitude lidar observation of planetary waves in the middle atmosphere during winter 1981-82, *J. Geophys. Res., 88,* 3843-3849, 1983.

Hauchecorne A., M. L. Chanin, and R. Wilson, Mesospheric temperature inversion and gravity wave breaking, *Geophys. Res. Mt.,* 14,933-936, 1987.

Hervig, M. E., J. M. Russell, L. L. Gordley, S. R. Drayson, K. Stone, R. E. Thompson, M. E. Gelman, 1. S. McDermid, A. Hauchecorne, P. Keckhut, T. J. McGee, U. N. Singh, and M. R. Gross, *J. Geophys. Res., 101, 10,277-10,286, 1996.*

Keckhut P., A. Hauchecorne, and M. L. Chanin, A critical review of the database acquired for the long-term surveillance of the middle atmosphere by French Rayleigh lidars, *J. Atm. Ocean. Technol., 10,* 850-867, 1993,

Keckhut P., Gelmann M. E., Wild J. D., Tissot F., Miller A. J., Hauchecorne A., Chanin M.-L., Fishbein E. F., Gille J., Russell III J. M., and Taylor F. W., Semi-diurnal and diurnal tides (30-55 km): Climatology and effect on UARS-LIDAR data comparisons, *J. Geophys. Res.,* **101,** 10299-10310, 1996,

Kurylo M. J., and S. Solomon, Network for the Detection of Stratospheric Change: a status and implementation report, *NASA. Upper Atmosphere Research Program and NOAA Climate and Global Change Program,* NASA, Washington D. C., 1990.

Leblanc T., A. Hauchecorne, M. L. Chanin, F. W. Taylor, C. D. Rodgers, and N. Livesey, Mesospheric temperature inversions as seen by ISAMS (UARS), *Geophys. Res. Z-MI.,* 22, 1485-1488, 1995.

Leblanc T., and A. Hauchecorne, Recent observations of the mesospheric temperature inversions, *J. Geophys. Res., submitted, 1997.*

Moskowitz, W. P., G. Davidson, D. Sipler, C. R. Philbrick, and P. Dao, Raman augmentation for Rayleigh lidar, 14th ILRC, Conference Abstracts, 284-286, 1988.

Singh U. N., Keckhut P., McGee T. J., Gross M. R., Hauchecorne A., Fishbein E. F., Waters J. W., Gille J., Roche A. E., and Russell III J. M., Stratospheric temperature measurements by two collocated NDSC lidars during UARS validation campaign, *J. Geophys. Res.,* **101,** 10287-10298, 1996.

Whiteway J. A., A. I. Carswell, and W. E. Ward, Mesospheric temperature inversions with overlying nearly adiabatic lapse rate an indication of a well-mixed turbulent layer, *Geophys. Res. Lett.,* 22, 1201-1204, 1995.

Wild, J. D., M. E. Gelman, A. J. Miller, M. L. Chanin, A. Hauchecorne, P. Keckhut, R. Farley, P. D. Dao, J. W. Meriwether, G. P. Gobbi, F. Congeduti, A. Adriani, I. S. McDermid, T. J. McGee, and E. F. Fishbein, *J. Geophys. Res., 100, 11,105-11,111,* 1995.

Wilson R., M. L. Chanin, and A. Hauchecorne, Gravity waves in the middle atmosphere by Rayleigh lidar, Part 1: Case studies, *J. Geophys. Res.*, 96,5153-5167, 1991a.

Wilson R., M. L. Chanin, and A. Hauchecorne, Gravity waves in the middle atmosphere by Rayleigh lidar, Part 2: Climatology, *J. Geophys. Res.*, 96,5169-5183, 1991 b.